




PORFLO Simulations of Loviisa Horizontal Steam Generator

Authors: Ville Hovi, Mikko Ilvonen

Confidentiality: Public

Report's title PORFLO Simulations of Loviisa Horizontal Steam Generator	
Customer, contact person, address VTT	Order reference
Project name Horizontal SG	Project number/Short name 30153
Author(s) Ville Hovi, Mikko Ilvonen	Pages 34/
Keywords horizontal steam generator, VVER-440, CFD, porosity model	Report identification code VTT-R-01406-10
Summary <p>Detailed simulations of large industrial components, such as steam generators, are currently not feasible using conventional CFD modeling. A model of the secondary side of a Loviisa VVER-440 horizontal steam generator was developed for PORFLO, a three-dimensional flow solver developed at VTT based on porous medium modeling. The necessary input data, in this case the outer temperatures of the primary tubes were chosen, was predicted by a model developed for APROS, a one-dimensional system code developed by VTT and Fortum. The governing equations and closure laws used in PORFLO are discussed, the APROS and PORFLO models and their coupling are briefly described, and the steady-state results of a full power level (250 MW) simulation are presented and compared to analogous Fluent simulations conducted in project SGEN.</p> <p>The results are, in general, in quite good agreement. However, the most distinct differences between the results of the two codes, one being the non-monotonicity of the void fraction distribution near the water surface predicted by PORFLO, pointed out some aspects of the PORFLO code that need further development in near future. This is not to say that the Fluent results are considered to be flawless either.</p>	
Confidentiality	Public
Espoo 17.2.2010	
Signatures 	Signatures 
Written by Ville Hovi, Research Scientist	Reviewed by Elina Syrjälähti Research Scientist
	Signatures 
	Accepted by Timo Vanttola Technology Manager
VTT's contact address VTT, PL 1000, FIN-02044 VTT	
Distribution (customer and VTT) SAFIR2010 Reference group 3, TK5012, Eija Puska (VTT), Timo Pättikangas (VTT), Timo Toppila (Fortum), Tommi Rämä (Fortum)	
<i>The use of the name of the VTT Technical Research Centre of Finland (VTT) in advertising or publication in part of this report is only permissible with written authorisation from the VTT Technical Research Centre of Finland.</i>	

Report's title PORFLO Simulations of Loviisa Horizontal Steam Generator		
Customer, contact person, address VTT		Order reference
Project name Horizontal SG		Project number/Short name 30153
Author(s) Ville Hovi, Mikko Ilvonen		Pages 34/
Keywords horizontal steam generator, VVER-440, CFD, porosity model		Report identification code VTT-R-01406-10
Summary <p>Detailed simulations of large industrial components, such as steam generators, are currently not feasible using conventional CFD modeling. A model of the secondary side of a Loviisa VVER-440 horizontal steam generator was developed for PORFLO, a three-dimensional flow solver developed at VTT based on porous medium modeling. The necessary input data, in this case the outer temperatures of the primary tubes were chosen, was predicted by a model developed for APROS, a one-dimensional system code developed by VTT and Fortum. The governing equations and closure laws used in PORFLO are discussed, the APROS and PORFLO models and their coupling are briefly described, and the steady-state results of a full power level (250 MW) simulation are presented and compared to analogous Fluent simulations conducted in project SGEN.</p> <p>The results are, in general, in quite good agreement. However, the most distinct differences between the results of the two codes, one being the non-monotonicity of the void fraction distribution near the water surface predicted by PORFLO, pointed out some aspects of the PORFLO code that need further development in near future. This is not to say that the Fluent results are considered to be flawless either.</p>		
Confidentiality	Public	
Espoo 18.2.2010		
Signatures	Signatures	Signatures
Written by Ville Hovi, Research Scientist	Reviewed by Elina Syrjälähti Research Scientist	Accepted by Timo Vanttola Technology Manager
VTT's contact address VTT, PL 1000, FIN-02044 VTT		
Distribution (customer and VTT) SAFIR2010 Reference group 3, TK5012, Eija Puska (VTT), Timo Pättikangas (VTT), Timo Toppila (Fortum), Tommi Rämä (Fortum)		
<i>The use of the name of the VTT Technical Research Centre of Finland (VTT) in advertising or publication in part of this report is only permissible with written authorisation from the VTT Technical Research Centre of Finland.</i>		

Contents

1	Introduction.....	6
2	Governing equations	6
3	Mass source terms	8
4	Momentum source terms.....	9
4.1	Interphase drag force between vapor and liquid	9
4.2	Drag force caused by the tube bundles	10
4.3	Momentum exchange due to phase change	12
5	Energy source terms	12
5.1	Heat transfer from the primary circuit.....	13
5.2	Bulk evaporation and condensation	15
5.3	Heat transfer between vapor and liquid	15
6	Model of the horizontal steam generator	16
6.1	APROS model of the steam generator.....	16
6.2	PORFLO model of the steam generator	18
6.3	APROS-PORFLO coupling	22
7	Simulation results	25
8	Discussion of results.....	31
9	Comparison of results to Fluent simulations	32
	References	34

Latin symbols:

A_s	Outer surface area of the tubes of the primary circuit	$[m^2]$
C_D	Drag coefficient	$[-]$
D_B	Bubble diameter	$[m]$
D_e	Equivalent diameter	$[m]$
D_t	Outer diameter of the tubes	$[m]$
Eu	Euler number	$[-]$
f	Friction coefficient	$[-]$
$F_{D,g}$	Drag force exerted on the vapor phase by tubes (per unit volume)	$[N/m^3]$
$F_{D,l}$	Drag force exerted on the liquid phase by tubes (per unit volume)	$[N/m^3]$
F_{id}	Interphase drag force (per unit volume)	$[N/m^3]$
F_{pc}	Momentum exchange due to phase change	$[N/m^3]$
g, g	Acceleration of gravity	$[m/s^2]$
h	Specific enthalpy	$[J/kg]$
h_{fg}	Latent heat of evaporation	$[J/kg]$
h_g	Specific vapor enthalpy	$[J/kg]$
h_l	Specific liquid enthalpy	$[J/kg]$
h'	Liquid saturation enthalpy	$[J/kg]$
h''	Vapor saturation enthalpy	$[J/kg]$
h'''_{RM}	Volumetric heat transfer coefficient for convection from vapor to liquid (Ranz-Marshall)	$[W/m^3K]$
h''_{wb}	Surface heat transfer coefficient for boiling	$[W/m^2K]$
h'''_{wb}	Volumetric heat transfer coefficient for boiling	$[W/m^3K]$
h''_{wg}	Surface heat transfer coefficient for convection into vapor	$[W/m^2K]$
h''_{wl}	Surface heat transfer coefficient for convection into liquid	$[W/m^2K]$
h'''_{wl}	Volumetric heat transfer coefficient for convection into liquid	$[W/m^3K]$
k	Thermal conductivity	$[W/mK]$
m	Model exponent of the tube friction correlations	$[-]$
\dot{m}_{lg}	Mass transfer rate per unit volume from liquid to vapor due to bulk evaporation	$[kg/m^3]$
\dot{m}_{gl}	Mass transfer rate per unit volume from vapor to liquid due to bulk condensation	$[kg/m^3]$
$\dot{m}_{lg,PR}$	Mass transfer rate per unit volume from liquid to vapor due to the heat transferred from the primary circuit (evaporation)	$[kg/m^3]$
$\dot{m}_{gl,PR}$	Mass transfer rate per unit volume from vapor to liquid due to the heat transferred from the primary circuit (condensation)	$[kg/m^3]$
n	Model exponent of the tube friction correlations	$[-]$
Nu	Nusselt number	$[-]$
p	Pressure	$[Pa]$
P	Pitch	$[m]$
Pr	Prandtl number	$[-]$
Re	Reynolds number	$[-]$
$q'''_{EC,g}$	Volumetric heat flux into vapor (due to bulk evaporation/ condensation)	$[W/m^3]$
$q'''_{EC,l}$	Volumetric heat flux into liquid (due to bulk evaporation/ condensation)	$[W/m^3]$

$q'''_{PR,g}$	Volumetric heat flux from primary tubes to vapor	[W/m ³]
$q'''_{PR,l}$	Volumetric heat flux from primary tubes to liquid	[W/m ³]
q'''_{RM}	Volumetric heat flux from vapor to liquid	[W/m ³]
q'''_{wb}	Volumetric heat flux (boiling heat transfer)	[W/m ³]
q'''_{wg}	Volumetric heat flux (convective heat transfer into vapor)	[W/m ³]
q'''_{wl}	Volumetric heat flux (convective heat transfer into liquid)	[W/m ³]
S_g	Energy sources per unit volume for vapor	[W/m ³]
S_l	Energy sources per unit volume for liquid	[W/m ³]
T	Temperature	[K]
\mathbf{T}	Surface force tensor (of rank 2)	[N/m ²]
t	Time	[s]
\mathbf{u}_g	Vapor velocity	[m/s]
\mathbf{u}_l	Liquid velocity	[m/s]
V_{fluid}	Fluid volume of a node, $V_{fluid} = \varepsilon V_{tot}$	[m ³]
V_{tot}	Total volume of a node	[m ³]
z	Number of tube rows in the node (in vertical direction)	[-]

Greek symbols:

α	Void fraction (vapor fraction of fluid volume)	[-]
β	Linear ramp function	[-]
γ	Evaporation / condensation rate per unit volume	[kg/m ³ s]
Δp	Pressure loss	[Pa]
Δz	Length of the calculation node (in vertical direction)	[m]
$\Delta \rho$	The difference between liquid and vapor density	[kg/m ³]
ε	Porosity (fluid fraction of total volume)	[-]
ζ	Friction coefficient	[1/m]
μ	Dynamic (molecular) viscosity	[Ns/m ²]
ρ	Density	[kg/m ³]
σ	Surface tension	[N/m]
τ_c	Time constant for bulk condensation	[s]
τ_e	Time constant for bulk evaporation	[s]

Subscripts:

b	Boiling
B	Bubble
c	Condensation
D	Drag
e	Evaporation or equivalent
EC	Evaporation and/or condensation
fg	Latent
g	Vapor
id	Interphase drag
l	Liquid
m	Mixture
pc	Phase change
PR	Primary (tubes)

<i>q</i>	Phase index: l for liquid and g for vapor
r	Relative
R	Ramp
RM	Ranz-Marshall
s	Surface
t	Tubes
tot	Total
w	Wall

Abbreviations:

CFD	Computational Fluid Dynamics
PWR	Pressurized Water Reactor
SG	Steam Generator

1 Introduction

In pressurized water reactors (PWR) the primary and secondary circuits are connected by steam generators, in which the heat from the primary circuit is used to produce steam on the secondary side of the steam generator. The steam is then conducted to turbines in which the heat energy is changed into mechanical energy and further into electricity in the generators. Two types of PWR steam generators exist: vertical steam generators, which are used in most of the Western reactors, and horizontal steam generators, which are used in most of the VVER-type plants. This work is related to general PORFLO development (Ilvonen and Hovi, 2010).

2 Governing equations

The six-equation model of PORFLO is based on conservation equations of mass, momentum and energy, written for both liquid and vapor phases.

Liquid mass conservation:

$$\frac{\partial[\varepsilon(1-\alpha)\rho_l]}{\partial t} + \nabla \cdot [\varepsilon(1-\alpha)\rho_l \mathbf{u}_l] = -\gamma \quad (2.1)$$

where

t	time [s],
\mathbf{u}_l	liquid velocity vector, whose components (u, v, w) [m/s],
α	void fraction (vapor fraction of fluid volume) [-],
ε	porosity (fluid fraction of total volume) [-],
ρ_l	liquid density [kg/m ³] and
γ	evaporation / condensation rate per unit volume [kg/m ³ s].

Vapor mass conservation:

$$\frac{\partial(\varepsilon\alpha\rho_g)}{\partial t} + \nabla \cdot (\varepsilon\alpha\rho_g \mathbf{u}_g) = +\gamma \quad (2.2)$$

where

\mathbf{u}_g	vapor velocity vector, whose components (u, v, w) [m/s] and
ρ_g	vapor density [kg/m ³].

Liquid momentum:

$$\frac{\partial[\varepsilon(1-\alpha)\rho_l \mathbf{u}_l]}{\partial t} + \nabla \cdot \{[\varepsilon(1-\alpha)\rho_l \mathbf{u}_l] \otimes \mathbf{u}_l\} = -\varepsilon(1-\alpha)\nabla p + \varepsilon(1-\alpha)\nabla \cdot \mathbf{T} + \varepsilon(1-\alpha)\rho_l \mathbf{g} + \mathbf{F}_{pc} + \mathbf{F}_{id} + \mathbf{F}_{D,l} \quad (2.3)$$

where

$\mathbf{F}_{D,l}$	drag force exerted on the liquid phase by tubes (per unit volume) [N/m ³],
\mathbf{F}_{id}	interfacial drag force (per unit volume) [N/m ³],

\mathbf{F}_{pc}	momentum exchange due to phase change [N/m^3],
\mathbf{g}	acceleration of gravity [m/s^2],
p	pressure [N/m^2],
\mathbf{T}	surface force (in this case viscous stress) tensor (of rank 2) [N/m^2], $[\nabla \cdot \mathbf{T}] = \text{N}/\text{m}^3$ and
\otimes	outer product.

Vapor momentum:

$$\frac{\partial(\varepsilon\alpha\rho_g\mathbf{u}_g)}{\partial t} + \nabla \cdot [(\varepsilon\alpha\rho_g\mathbf{u}_g) \otimes \mathbf{u}_g] = -\varepsilon\alpha\nabla p + \varepsilon\alpha\rho_g\mathbf{g} - \mathbf{F}_{pc} - \mathbf{F}_{id} + \mathbf{F}_{D,g} \quad (2.4)$$

where $\mathbf{F}_{D,g}$ drag force exerted on the vapor phase by tubes (per unit volume) [N/m^3].

At present the momentum equations only contain interfacial drag, the drag caused by the tube bundles (as a pressure loss term) and the momentum exchange due to phase change. Lift force and virtual mass force have been neglected, since they have been considered to be insignificant in this application.

The effect of diffusion in the vapor momentum equations has been neglected due to the fact that vapor is the dispersed phase throughout most of the calculation domain, and hence the effect of diffusion is less significant in conservation of vapor momentum, than in liquid momentum. Once a turbulence model is introduced, the effect of diffusion might have to be included in the vapor momentum equations as well, since turbulent viscosity is in many cases far greater than molecular viscosity. Then, for both liquid and vapor, the surface force tensor, \mathbf{T} , would contain the sum of molecular and turbulent viscosities.

Liquid energy:

$$\frac{\partial[\varepsilon(1-\alpha)\rho_l h_l]}{\partial t} + \nabla \cdot [\varepsilon(1-\alpha)\rho_l h_l \mathbf{u}_l] = S_l \quad (2.5)$$

where h_l (specific) liquid enthalpy [J/kg] and
 S_l Energy sources per unit volume for liquid [W/m^3].

Vapor energy:

$$\frac{\partial(\varepsilon\alpha\rho_g h_g)}{\partial t} + \nabla \cdot (\varepsilon\alpha\rho_g h_g \mathbf{u}_g) = S_g \quad (2.6)$$

where h_g (specific) vapor enthalpy [J/kg] and
 S_g Energy sources per unit volume for vapor [W/m^3].

3 Mass source terms

Mass transfer between the phases is included as a source term in the continuity equations of both phases. The mass transfer rate from liquid to vapor per unit volume, γ , is given through the following relation.

$$\gamma = \dot{m}_{lg} - \dot{m}_{gl} + \dot{m}_{lg,PR} - \dot{m}_{gl,PR} \quad (3.1)$$

where

\dot{m}_{lg}	mass transfer rate per unit volume from liquid to vapor due to bulk evaporation [kg/m ³],
\dot{m}_{gl}	mass transfer rate per unit volume from vapor to liquid due to bulk condensation [kg/m ³],
$\dot{m}_{lg,PR}$	mass transfer rate per unit volume from liquid to vapor due to the heat transferred from the primary circuit (evaporation) [kg/m ³],
$\dot{m}_{gl,PR}$	mass transfer rate per unit volume from vapor to liquid due to the heat transferred from the primary circuit (condensation) [kg/m ³].

Bulk evaporation occurs, when liquid enthalpy is higher than liquid saturation enthalpy, i.e., $h_1 > h'$, whereas bulk condensation occurs, when vapor is in contact with subcooled liquid, i.e., $h_1 < h'$. The following correlations are used for bulk evaporation and condensation

$$\begin{aligned} \text{evaporation : } \dot{m}_{lg} &= \frac{(1-\alpha)\rho_1}{\tau_e} \frac{h' - h_1}{h'' - h'} \\ \text{condensation : } \dot{m}_{gl} &= \frac{(1-\alpha)\rho_1}{\tau_c} \frac{h_1 - h'}{h'' - h'} \end{aligned} \quad (3.2)$$

where

h'	liquid saturation enthalpy [J/kg],
h''	vapor saturation enthalpy [J/kg],
h_1	liquid enthalpy [J/kg],
τ_c	time constant for bulk condensation [s] and
τ_e	time constant for bulk evaporation [s].

Constant values of 1 s have been used for both the evaporation and condensation time constants. The evaporation and condensation time constants, in essence, represent the return to saturation time scale; the time it takes to reach thermodynamic equilibrium.

Mass transfer due to the primary circuit, $\dot{m}_{lg,PR}$ and $\dot{m}_{gl,PR}$, is discussed in Section 5.1.

4 Momentum source terms

The momentum source terms, in equations (2.3) and (2.4), are discussed in more detail in this section. The following source terms were used in the simulations of the horizontal steam generator.

4.1 Interphase drag force between vapor and liquid

Calculation of the interfacial drag force is crucial, since it dictates the velocity difference between the phases, also known as phase separation. For dispersed vapor bubbles in liquid the interfacial drag force is of the form

$$\mathbf{F}_{id} = \frac{3}{4} \alpha \rho_l \frac{C_D}{D_B} |\mathbf{u}_g - \mathbf{u}_l| (\mathbf{u}_g - \mathbf{u}_l) \quad (4.1)$$

where C_D interfacial drag coefficient [-],
 D_B bubble diameter [m] and
 \mathbf{F}_{id} interphase drag force per unit volume [N/m^3].

The correlations for the ratio of interfacial drag coefficient and bubble diameter are taken according to the presentation of Simovic, Ockoljic and Stevanovic (2007). The correlation proposed consists of two parts. The first part, valid for bubbly flow regime ($\alpha < 0.3$), has been adopted from Ishii and Zuber (1979), in which the authors have introduced a minor modification: the original correlation is multiplied by a factor 0.4, to make a better fit for their experimental data, which was bubbly flow over a horizontal tube bundle.

$$\frac{C_D}{D_B} = 0.267 \left(\frac{g \Delta \rho}{\sigma} \right)^{\frac{1}{2}} \left[\frac{1 + 17.67 f(\alpha)^{\frac{6}{7}}}{18.67 f(\alpha)} \right]^2 \quad (4.2)$$

where g acceleration of gravity [m/s^2],
 $\Delta \rho$ the difference between liquid and vapor density [kg/m^3],
 σ surface tension [N/m] and
 $f(\alpha)$ the dependence on void fraction as follows

$$f(\alpha) = (1 - \alpha)^{\frac{3}{2}} \quad (4.3)$$

The second part of the correlation for churn-turbulent flows, ($\alpha > 0.3$), is given through

$$\frac{C_D}{D_B} = 1.487 \left(\frac{g \Delta \rho}{\sigma} \right)^{\frac{1}{2}} (1 - \alpha)^3 (1 - 0.75\alpha)^2 \quad (4.4)$$

where according to Simovic, Ocokoljic and Stevanovic the dependence on void fraction has the same form as the CATHARE code. The dependence of the ratio of interphase drag coefficient and bubble diameter on void fraction is presented in Figure 4.1.

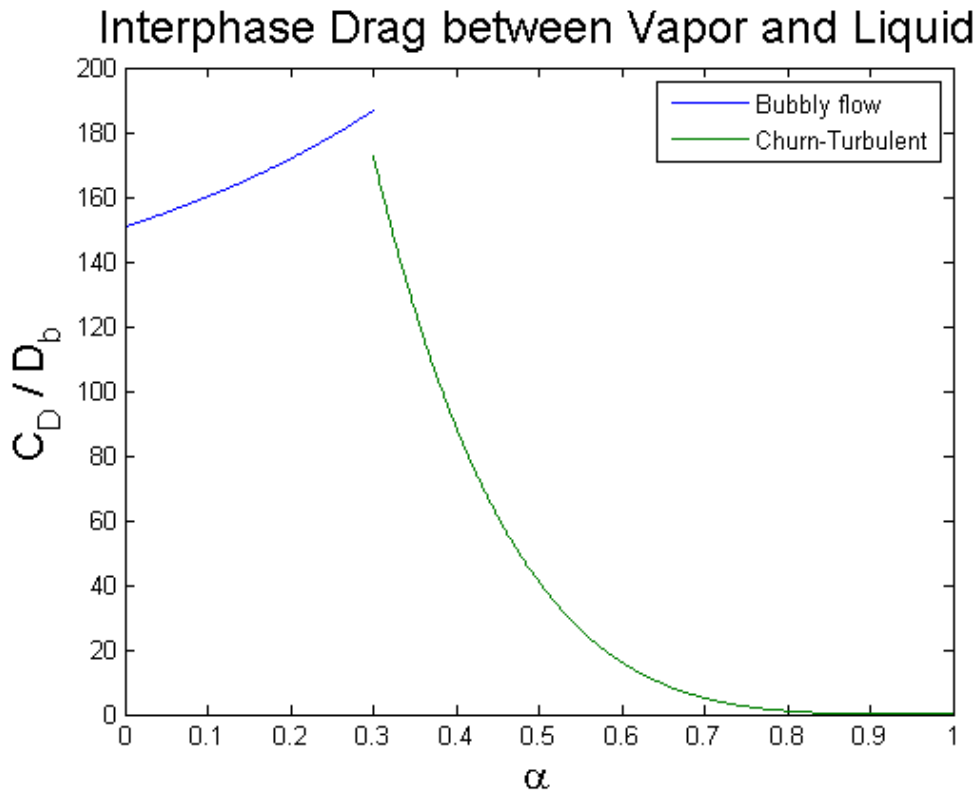


Figure 4.1: Interphase friction.

It is seen from Figure 4.1 that the lines do not actually join. This lead to oscillations inside the SIMPLE iteration, which in turn caused the SIMPLE iterations to stagnate, when the choice between the two parts of the correlation was made based on the implicitly calculated void fraction (at the end of the time step). As a solution to this the choice between the two parts of the correlation is now made based on the local void fraction at the beginning of the time step, which doesn't change between iterations. Another remedy would be to smooth the transition between the two parts of the correlation, and then the implicitly calculated void fraction could be used as the deciding parameter.

4.2 Drag force caused by the tube bundles

The drag force caused by the tube bundles consists of two parts: a viscous loss term proportional to velocity and an inertial loss term proportional to the square of velocity. The viscous loss term can often be ignored when velocities are sufficiently high. The drag force, without the linear viscous term, per unit volume can be expressed as follows

$$\mathbf{F}_{D,q} = -\frac{1}{2} \frac{f_q}{D_e} \alpha_q \rho_q |\mathbf{u}_q| \mathbf{u}_q \quad (4.5)$$

where D_e equivalent diameter [m],
 f_q friction coefficient of phase q [-],
 $\mathbf{F}_{D,q}$ drag force caused by the tube bundles on phase q [N/m³] and
 q phase index: l for liquid and g for vapor.

The dimensionless Euler number, Eu , expresses the relation between a local pressure drop over a restriction and kinetic energy per volume:

$$Eu = \frac{\Delta p}{\rho u^2} \quad \Leftrightarrow \quad \Delta p = Eu \rho u^2 \quad (4.6)$$

The pressure drops can be written for both phases separately:

$$\begin{aligned} \text{liquid: } \Delta p_1 &= Eu_1 \rho_1 u_1^2 (1 - \alpha) \\ \text{vapor: } \Delta p_2 &= Eu_2 \rho_2 u_2^2 \alpha \end{aligned} \quad (4.7)$$

The drag forces per unit volume can be calculated by dividing the pressure drops by the length of the calculation node, Δz , and multiplying by the porosity of the bundle, ε , since the pressure differences act over the fluid area.

$$\begin{aligned} \text{liquid: } \mathbf{F}_{D,l} &= -\frac{Eu_1 \rho_1 |\mathbf{u}_l| \mathbf{u}_l \varepsilon (1 - \alpha)}{\Delta z} \\ \text{vapor: } \mathbf{F}_{D,g} &= -\frac{Eu_2 \rho_2 |\mathbf{u}_g| \mathbf{u}_g \varepsilon \alpha}{\Delta z} \end{aligned} \quad (4.8)$$

The Euler numbers are calculated according to the presentation of Simovic, Ocokoljic and Stevanovic (2007, Appendix A) for equilateral in-line tubes arrangement:

$$Eu_q = 0.265 \left(\frac{\frac{P}{D_t} - 0.8}{\frac{P}{D_t} - 1} \right)^n z Re_q^m \quad (4.9)$$

where D_t diameter of the tubes [m],
 P pitch [m],
 Re_q Reynolds number for phase q [-],
 z the number of tube rows in the node; $\Delta z / P$ [-],
 m and n exponents [-] given through the following relations:

$$n = \begin{cases} 2.5 & \text{for } \frac{\frac{P}{D_t} - 0.8}{\frac{P}{D_t} - 1} \leq 1 \\ 2.0 & \text{for } \frac{\frac{P}{D_t} - 0.8}{\frac{P}{D_t} - 1} > 1 \end{cases} \quad (4.10)$$

$$m = \begin{cases} -0.133 & \text{for } \frac{P}{D_t} \geq 1.24 \\ 0.867 \left(\frac{P}{1.24 D_t} \right)^{0.7} - 1 & \text{for } \frac{P}{D_t} < 1.24 \end{cases} \quad (4.11)$$

4.3 Momentum exchange due to phase change

When phase change occurs, the momentum of the donating phase is transferred to the receiving phase. The relation used in PORFLO is quite simple, depending on the direction of the net phase change in the particular velocity node, whether net evaporation or condensation is occurring, the corresponding momentum, velocity [m/s] times the net evaporation or condensation rate per unit volume [kg/m³s], is subtracted from the donating phase and added to the receiving phase. The relation can be expressed as follows:

$$\mathbf{F}_{pc} = \max(-\gamma, 0) \mathbf{u}_g - \max(\gamma, 0) \mathbf{u}_l \quad (4.12)$$

where \mathbf{F}_{pc} momentum exchange due to phase change [kg m/s²] and
 γ net evaporation rate (+) or net condensation rate (-) per unit volume [kg/m³s].

5 Energy source terms

The energy source terms, in equations (2.5) and (2.6), are discussed in more detail in this section. The following source terms were used in the simulations of the horizontal steam generator for liquid and vapor, respectively:

$$S_l = q_{PR,l}''' + q_{EC,l}''' - q_{RM}''' \quad (5.1)$$

$$S_g = q_{PR,g}''' + q_{EC,g}''' + q_{RM}''' \quad (5.2)$$

5.1 Heat transfer from the primary circuit

The heat transfer modes between the heat transfer tubes and fluid include convective heat transfer to liquid, boiling heat transfer, if wall temperature is superheated ($T_w > T_{sat}$), and convective heat transfer to gas. During steady state operation, the main heat transfer modes are the forced convection into liquid and boiling heat transfer.

Using the volumetric heat transfer coefficient, h'''_{wl} , the volumetric heat flux can be expressed through

$$q'''_{wl} = h'''_{wl} (T_w - T_l) \quad (5.3)$$

In terms of the surface related heat transfer coefficient, h''_{wl} , we have

$$q'''_{wl} = h''_{wl} (T_w - T_l) \left(\frac{A_s}{V_{tot}} \right) (1 - \alpha) \quad (5.4)$$

The Dittus-Boelter correlation (Incropera and DeWitt, 2002, Section 8.5, p. 491) has been selected for the secondary side of the steam generator:

$$h''_{wl} = 0.023 \frac{k_l}{D_e} \text{Re}_m^{0.8} \text{Pr}_l^{0.4} \quad (5.5)$$

where the mixture Reynolds number is defined as

$$\text{Re}_m = \frac{\rho_m |\mathbf{v}_m| D_e}{\mu_l} \quad (5.6)$$

Mixture density and velocity are defined as volume averaged quantities.

The equivalent diameter for the complex bundle is derived from the fluid volume and surface area as

$$D_e = \frac{4V_{fluid}}{A_s} \quad (5.7)$$

When vapor is in contact with the heat transfer tubes convective heat transfer into the vapor phase is defined through

$$q'''_{wg} = h''_{wg} (T_w - T_g) \left(\frac{A_s}{V_{tot}} \right) \alpha \quad (5.8)$$

where the surface heat transfer coefficient h''_{wg} is again obtained from the Dittus-Boelter correlation, as follows

$$h''_{wg} = 0.023 \frac{k_g}{D_e} \text{Re}_m^{0.8} \text{Pr}_g^{0.4} \quad (5.9)$$

Boiling is added to the heat transfer, when the structure temperature exceeds the saturation temperature. An additional limiter, $(1-\alpha)^{0.1}$, has been included to limit the heat transfer at high void fractions. The volumetric boiling correlation reads

$$q'''_{wb} = h'''_{wb} \max(T_w - T_{sat}, 0) (1-\alpha)^{0.1} \quad (5.10)$$

In terms of a surface area heat transfer coefficient, the volumetric heat flux is

$$q'''_{wb} = h''_{wb} \max(T_w - T_{sat}, 0) (1-\alpha)^{0.1} \left(\frac{A_s}{V_{tot}} \right) \quad (5.11)$$

The surface area heat transfer coefficient is derived from Thom pool boiling correlation, for it is rather practical, since the heat transfer coefficient is only a function of pressure. Once the correlation presented in (Groeneveld and Snoek, 1986) is slightly modified (only to change the units), it reads

$$h''_{wb} = 1971.2 e^{0.023p} (T_w - T_{sat}) \quad (5.12)$$

Here the unit of pressure is bar and the surface heat transfer coefficient is in units of $\text{W}/\text{m}^2\text{K}$.

Since it is not specified in the pool boiling correlation which phase receives the heat transferred from the tubes, it has to be decided. An approach was selected in which the heat transfer is used, in its entirety, for liquid heating when liquid subcooling exceeds 20 K, for vapor generation when liquid is saturated or superheated, and between these two points, the heat transfer is split into two components using a linear ramp function.

$$\beta = \min \left[\max \left(\frac{T_{sat} - T_l}{20 \text{K}}, 0 \right), 1 \right] \quad (5.13)$$

The volumetric steam generation ($\text{kg}/\text{m}^3\text{s}$) is given by

$$\dot{m}_{lg,PR} = (1-\beta)(q'''_{wb} + q'''_{wl}) / h_{fg} \quad (5.14)$$

and the corresponding energy source term for vapor is

$$q'''_{PR,g} = \dot{m}_{lg,PR} h_{fg} + q'''_{wg} \quad (5.15)$$

The rest of the total heat flux used for liquid heating

$$q'''_{PR,l} = \beta (q'''_{wb} + q'''_{wl}) \quad (5.16)$$

The possibility that vapour condenses on the heat transfer tubes is ignored:

$$\dot{m}_{gl,PR} = 0 \quad (5.17)$$

5.2 Bulk evaporation and condensation

Bulk evaporation occurs, when liquid enthalpy is higher than liquid saturation enthalpy, i.e., $h_1 > h'$, whereas bulk condensation occurs, when vapor is in contact with subcooled liquid, i.e., $h_1 < h'$. Once the mass source terms are calculated according to equation (3.2) the corresponding energy source terms, in equations (5.1) and (5.2), for liquid and vapor, respectively, are given through

$$q_{EC,l}''' = (\dot{m}_{gl} - \dot{m}_{lg})(h'' - h') \quad (5.18)$$

$$q_{EC,g}''' = (\dot{m}_{lg} - \dot{m}_{gl})(h'' - h') \quad (5.19)$$

where \dot{m}_{gl} denotes evaporation and \dot{m}_{lg} denotes condensation.

5.3 Heat transfer between vapor and liquid

Only vapor cooling is considered, since the bulk evaporation correlation accounts for the case in which liquid is superheated. The volumetric heat transfer rate from vapor to liquid can be expressed as follows

$$q_{RM}''' = h_{RM}'''(T_g - T_l) \quad (5.20)$$

where

h_{RM}'''	volumetric heat transfer coefficient (Ranz-Marshall) [W/m ³ K],
q_{RM}'''	volumetric heat transfer rate (from vapor to liquid) [W/m ³],
T_g	vapor temperature [K or °C],
T_l	liquid temperature [K or °C].

The volumetric heat transfer coefficient from vapor to liquid is given through

$$h_{RM}''' = \frac{6k_l\alpha(1-\alpha)Nu_l}{D_B^2} \quad (5.21)$$

where

D_B	bubble diameter [m],
k_l	thermal conductivity of liquid [W/mK] and
Nu_l	liquid Nusselt number, according to the Ranz-Marshall correlation:

$$\begin{cases} Nu_l = 2.0 + 0.6Re_r^{1/2} Pr_l^{1/3} \\ Re_r = \frac{\rho_l |\mathbf{u}_g - \mathbf{u}_l| D_b}{\mu_l} \end{cases} \quad (5.22)$$

where Re_r relative Reynolds number (for the bubble) [-] and

Pr_l liquid Prandtl number [-].

Since the relation does not account for phase changes, the volumetric heat transfer rate q_{RM}''' is set zero when vapor temperature is either below liquid temperature or vapor is saturated; the bulk evaporation and condensation correlations, presented in the previous section, are meant for this purpose instead.

6 Model of the horizontal steam generator

A model for a horizontal steam generator of a VVER-440 plant was developed using APROS, a system code developed by VTT and Fortum. The outer wall temperatures of the heat transfer tubes of the primary circuit were predicted using APROS and then used as an input for PORFLO. In the following subsections, the APROS and PORFLO models of the horizontal steam generator are presented and the APROS-PORFLO coupling is discussed briefly.

6.1 APROS model of the steam generator

The primary circuit has been divided into five (5) horizontal layers in the APROS model. The uppermost layer is presented in Figure 6.1. Several tubes are modeled with the same APROS component: four (4) consecutive tubes in the horizontal direction and fifteen (15) in the vertical direction. The flow rate of the primary circuit is controlled by a control valve and a control circuit.

The secondary side of the steam generator is presented in Figure 6.2. The portion of the secondary side occupied by the tube bundles has also been divided into five (5) horizontal layers. Five (5) horizontally aligned ‘downcomer’ nodes have been added to allow some recirculation, and the area above the tube bundles (steam dome) is modeled with two (2) nodes. The heat transferred in each of the five layers of the primary circuit is conveyed into its own node on the secondary side. The feed water flow is adjusted with a three-point control, which monitors the water level of the uppermost ‘downcomer’ node.

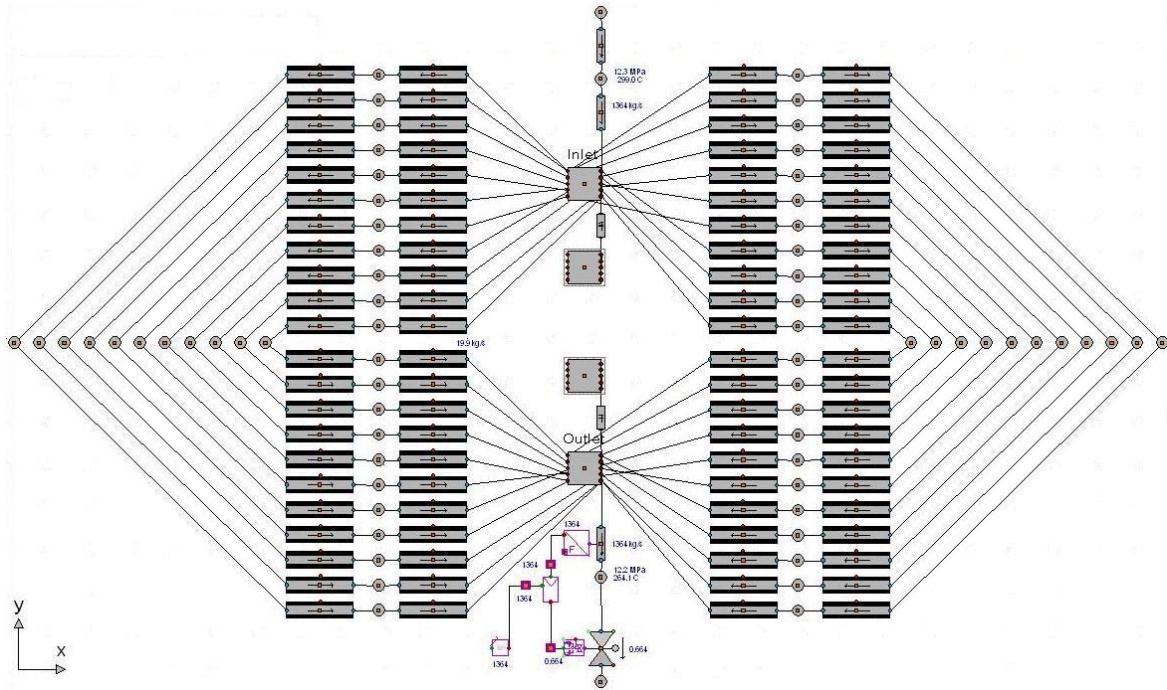


Figure 6.1: The uppermost level of the primary circuit in the APROS model.

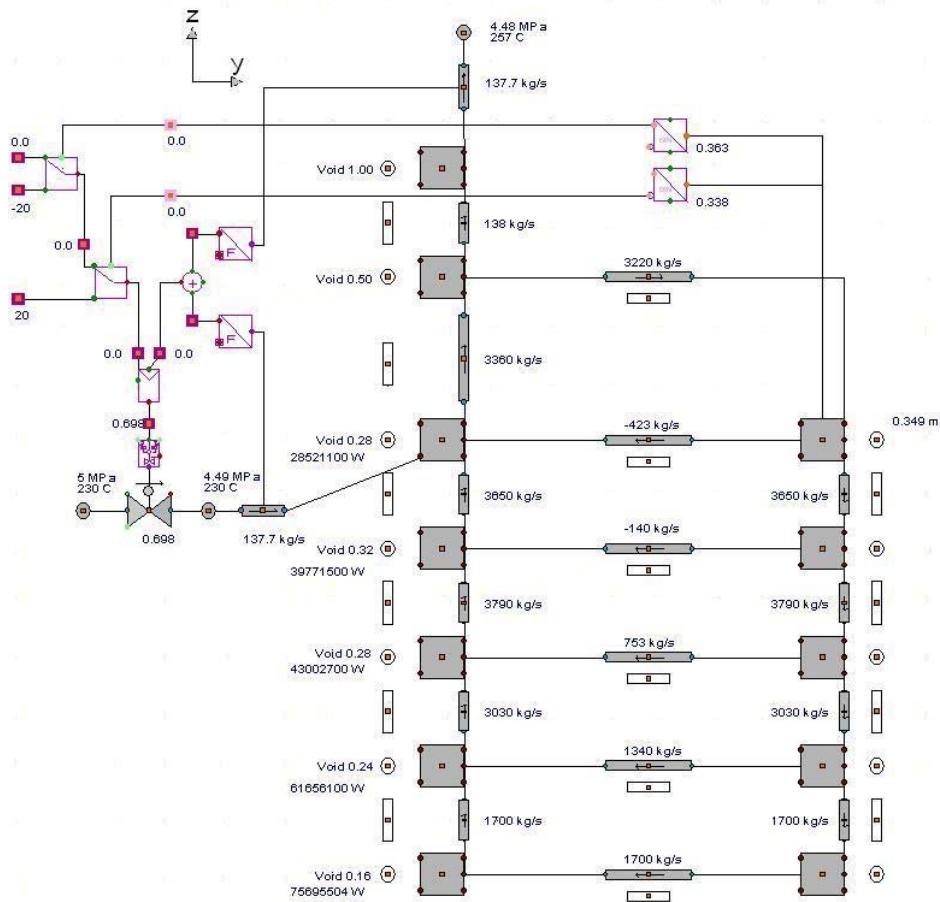


Figure 6.2: The secondary side of the APROS model.

6.2 PORFLO model of the steam generator

The Loviisa VVER-440 model 213 plant has 6 steam generators, which (unlike the usual western design) have the cylindrical shell in horizontal position rather than vertical. The inner volume of the shell is appr. 12 m long and its diameter is appr. 3 m. The ends of the cylinder are rounded, as can be seen in Figure 6.3 (Rämä, 2009). The internals of a horizontal steam generator have quite a complex geometry, including for example:

- 5536 tubes, in U tube form, inside which the primary circuit coolant flows
- two collectors whose function is to divide the primary circuit flow among the tubes (hot collector) or ‘collect’ the flow from the tubes (cold collector)
- feedwater injection tube, located (regarding the vertical direction) just above the tube bunches, between the bunches and the ‘steam dome’ volume (upper part of the cylinder)
- old feedwater injection tube, which is not in use and has been blocked
- vertical support plates, through which the tubes go and whose function is to keep them steady in the given distance grid by preventing vibrations due to boiling
- steam separator structure near the top of the volume
- at one end, a ladder attached to the inner side of the shell wall.

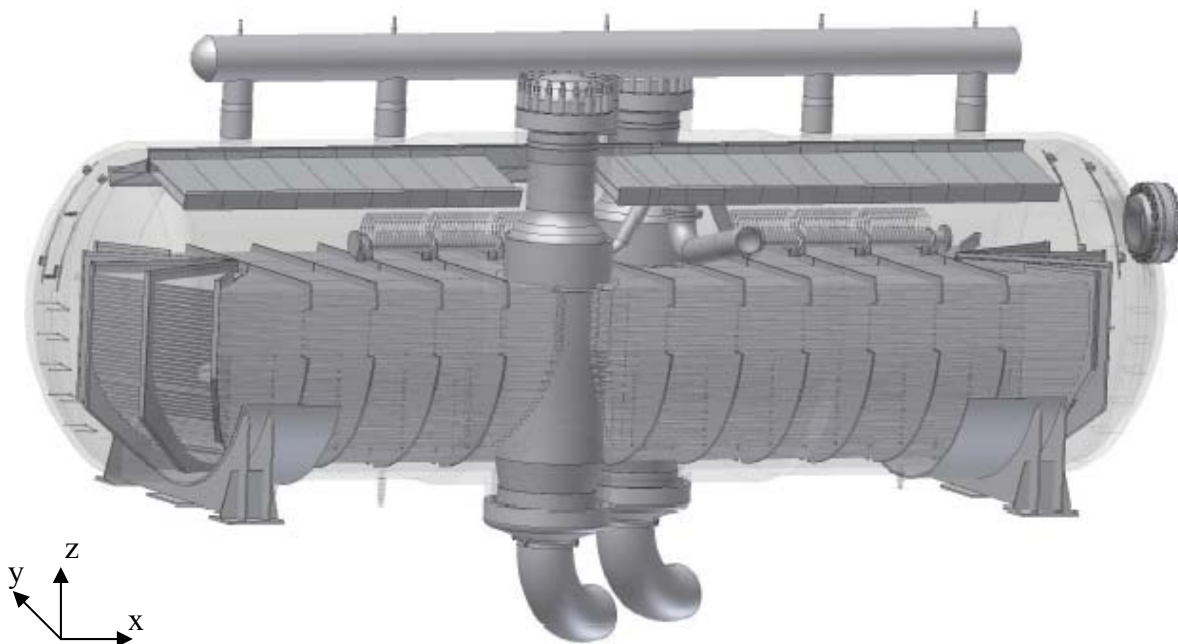


Figure 6.3: VVER-440 Horizontal steam generator (Rämä, 2009).

It is not possible with present CFD codes and present computing power to simulate the SG secondary side with a structure-fitted computational mesh, as a prohibitively large number of cells would be needed in order to fit all the walls of all the parts. This makes the SG an appropriate candidate for a simulation approach with porous medium modeling. For example,

typical Fluent calculations have the tube bunches described as a porous zone. In PORFLO, always with Cartesian coordinates, this is the only possible option.

In the present work, the geometry handling scheme was made with the objective of being able to express the geometry in arbitrary Cartesian nodalizations. For this reason, there is no one single fixed array containing the porosities (fraction of fluid volume of the cell total volume) and other information, but rather a subroutine which calculates this information for any given Cartesian grid during the initialization phase of a PORFLO simulation. The possible additional effort of programming such a piece of code can be justified by the fact that there are 12 such horizontal SGs in operation in Finland, and their operation will continue (as presently known) until at least year 2027. So they will continue to be an important object of future studies.

Of course, one has to bear in mind that even when arbitrary nodalizations are possible from the geometry handling point of view, they are not necessarily possible from the point of view of the physical models, correlations etc. used. There is a very big difference in modeling depending on e.g. whether several primary tubes fit into the cross-section of one grid cell (usual porous medium approach, the case in this work), or whether, in the other extreme, there would be several grid cells in a ‘subchannel’ between the tubes. The calculation of structure volume fractions and heated areas for grid cells are performed in a numerical fashion. Depending on how the chosen Cartesian grid happens to coincide with the tube grid, it is possible to produce uniform-looking porosity (good case) there or a checker board like pattern (not so good). In the following, a brief description is given on which details of the SG geometry are taken into account in the present work and which are not.

The shape of the rounded ends of the shell, as well as a lot of other data, was taken from a Fortum report (FNS-TERMO-43, Fig. A-2). The way to describe rounded shapes (walls and ends of the cylindrical shell) in PORFLO is to have some porosity in the cells through which the wall goes (cf. Figure 6.4 - 6.8), fluid only (porosity = 1) inside the shell and structure only (porosity = 0) in the outside.

The primary tubes form a relatively regular tube grid in the yz-plane (the circular cross-section of the cylinder in Figure 6.4). The main irregularities are due to the rounded shape of the shell walls, empty ‘gaps’ between tube bunches (with free vertical flow in the gap) and a larger ‘hollow’ empty space near the bottom level of the tube bunches. In the present work, the tubes are described as piecewise linear having long linear segments in the x-axis

(longitudinal) direction of the SG, and smaller pieces near the collectors as well as near the ends of the SG. The tubes are looped through one by one and it is checked piece by piece in which grid cell the piece is located. It is assumed here that the grid cells are clearly larger than tube diameter.

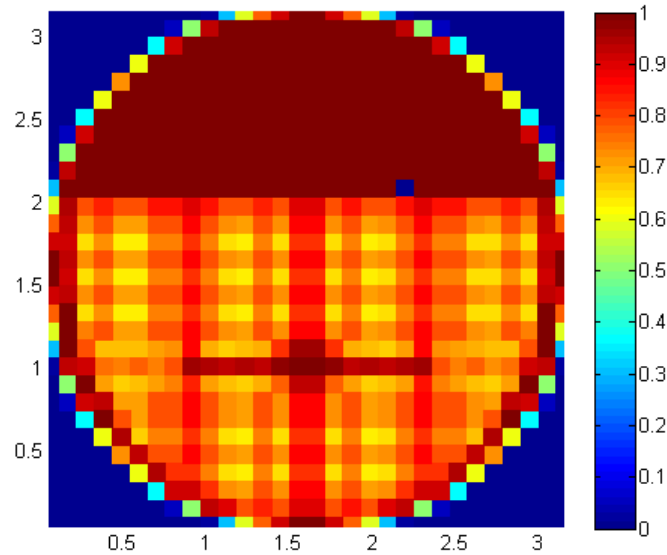


Figure 6.4: Porosity on yz-plane ($x = 3.10$ m).

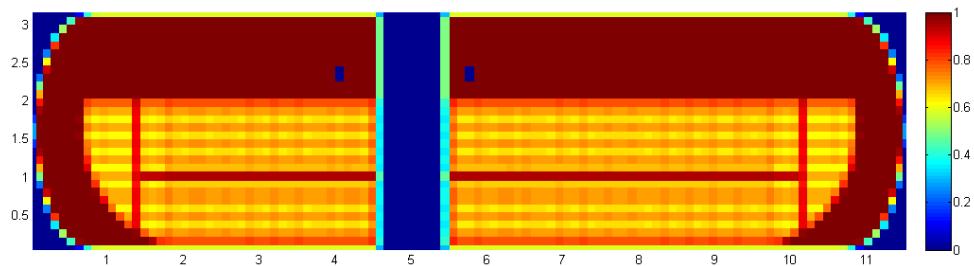


Figure 6.5: Porosity on xz-plane ($y = 2.00$ m).

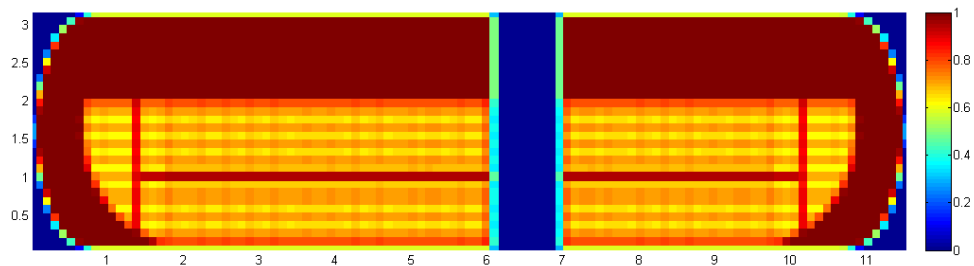


Figure 6.6: Porosity on xz-plane ($y = 1.21$ m).

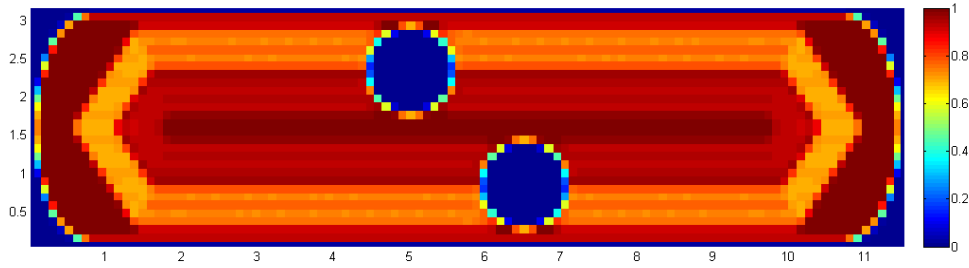


Figure 6.7: Porosity on xy-plane ($z = 1.00$ m).

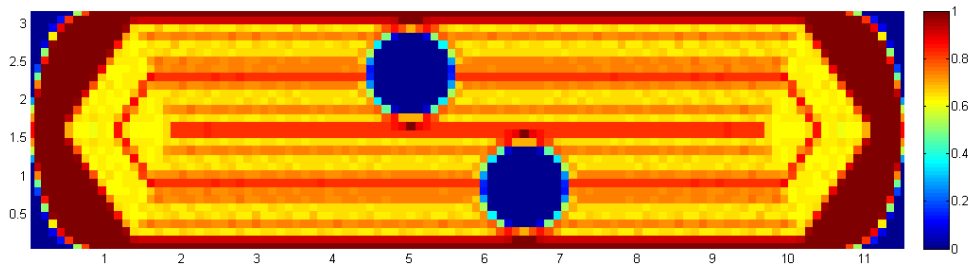


Figure 6.8: Porosity on xy-plane ($z = 1.50$ m).

The two collectors are described as vertical cylindrical objects which extend all the way through the SG. Presently they have constant radius, though in reality the radius changes with z (vertical) coordinate. This, like many other approximations, are only due to limited working time spent for the present work; there is no principal limitation to describe the geometry with all the details, apart from the fact that its representation in PORFLO will always be contained in the Cartesian grid, with the resolution of the grid. It must also be noted here that even when the porosity array as such does not contain any information on the shape or direction of the structures, it is well possible to utilize such information when developing the physical models (correlations and other).

The functioning feedwater pipe is described as piecewise linear. The feedwater is injected from the two longitudinal segments only. Some shorter segments make up the curve going around the collector. The numerical representation (volume subtracted from porosity and area injecting feedwater) is presently a rough approximation where those data are put to tube centerline cells only. It could easily be made better with some additional coding.

There are some structures which are at the time of this writing still missing from the model, like the old (blocked) feedwater pipe and the support plates. The plates are not easy to represent with the basic logic of porous medium approach. Instead, the grid should be made such that the plates would coincide with cell boundaries, and the plates would be taken into account separately when forming the equation systems to be solved.

6.3 APROS-PORFLO coupling

There are several ways in which a CFD code (like PORFLO) and a system code (like APROS) can be coupled, depending of course on what is being simulated. The transfer of information between the two codes can either be unidirectional, in which case the results of one code can be thought of as an input to the other, or bidirectional, in which case the codes either run simultaneously or successively, one after the other, and information is passed both ways between the two codes during the simulation.

“One-way coupling” is the obvious choice to begin with, but in essence it is really no coupling at all, since the problem (flow in the primary circuit – heat transfer – flow in the secondary circuit) is solved in its entirety with the first code, in this case APROS, and only a subsection of the problem (flow in the secondary side) is solved with the second code, in this case PORFLO. Therefore the limitations of the first code, the approximations made, the correlations used etc., are inherent in the data that is input to the second code. Only when the whole problem is split in two (say at the outer surfaces of the heat transfer tubes) and the first code handles one part of the problem (say flow solution of the primary circuit and heat transfer up to the outer surfaces of the tubes), the second code handles the other part of the problem (heat transfer from the outer surfaces of the tubes to the secondary circuit and the flow solution of the secondary circuit) and “two-way coupling” is used at the interface (surface temperatures are calculated by the first code and transferred to the second code which then calculates the corresponding heat flux and sends it back to the first code) are the two codes coupled in the true meaning of the word.

Due to the limited resources of this project “one-way coupling” was used. The outer wall temperatures of the heat transfer tubes of the primary circuit were first predicted using APROS and then transferred to PORFLO as input. A mapping routine was made for this purpose. First the temperature data, which is spatially quite coarse due to the fact that the nodes of the APROS model are quite large, was output to a text file. The form of the text file is essentially a list of temperatures at given points along the components that correspond to a small set of the primary tubes (or more precisely, a list of temperatures and the corresponding 3D Cartesian coordinates of that point). The second step was to augment this data set by linearly interpolating additional data points between two original data points that lie on the same component. The third step was to loop over each node of the 3D model, occupied by the primary tubes, and to select a sufficient amount of data points nearest to the center of the node

and obtain the temperature by interpolation. 2D cross-sections of the interpolated surface temperatures of the primary tubes are presented in Figures 6.9 - 6.13 and, to get an overview of the situation, a 3D representation (made with StarNode, whose author is Pasi Inkinen at VTT) of the surface temperatures is shown in Figure 6.14.

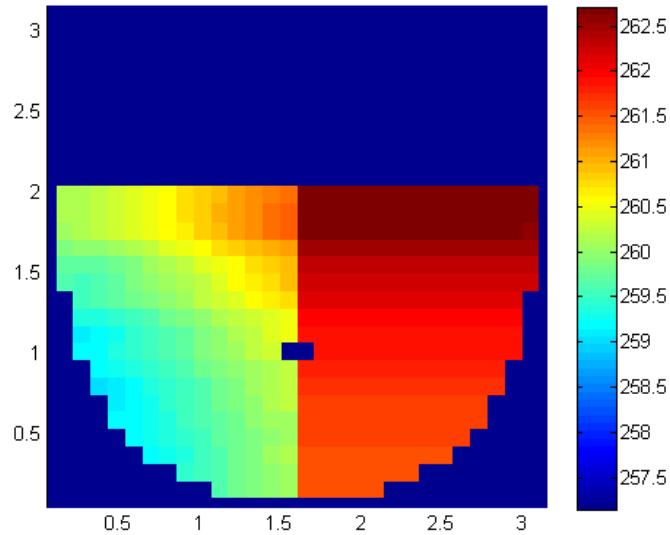


Figure 6.9: Surface temperature on yz-plane ($x = 3.10$ m) [$^{\circ}\text{C}$].

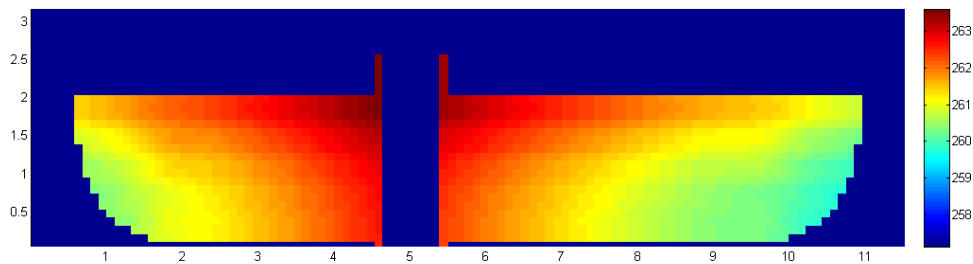


Figure 6.10: Surface temperature on xz-plane ($y = 2.00$ m) [$^{\circ}\text{C}$].

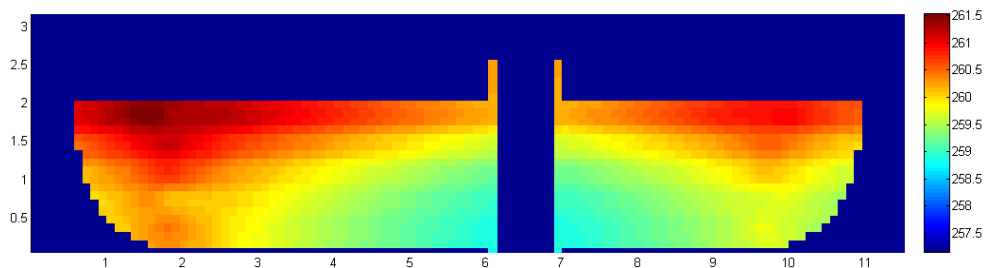


Figure 6.11: Surface temperatures on xz-plane ($y = 1.21$ m) [$^{\circ}\text{C}$].

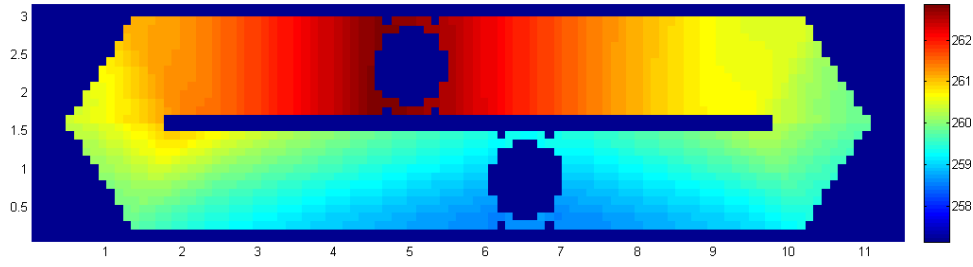


Figure 6.12: Surface temperatures on xy-plane ($z = 1.00$ m) [$^{\circ}\text{C}$].

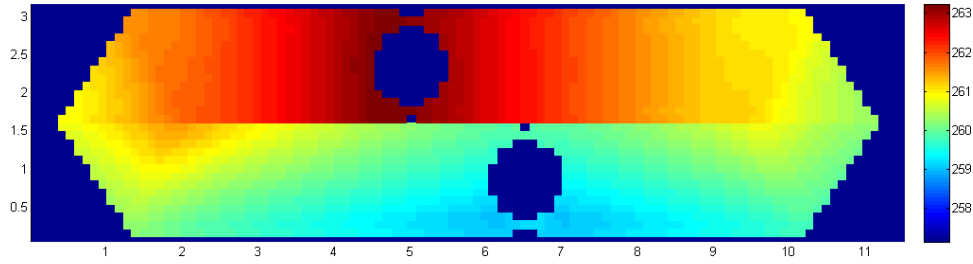


Figure 6.13: Surface temperatures on xy-plane ($z = 1.50$ m) [$^{\circ}\text{C}$].

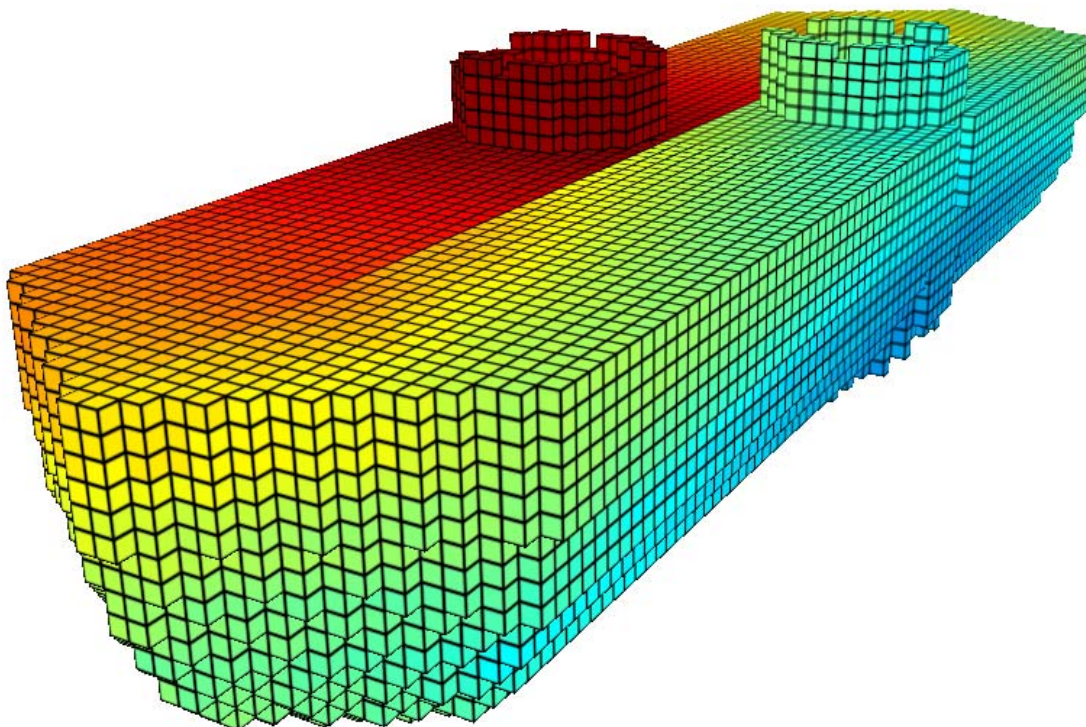


Figure 6.14: A 3D representation of the surface temperatures.

7 Simulation results

The objective was to simulate the steady-state of normal operation (approximately 250 MW for each SG). The procedure was such that the simulation was run as a transient, with fixed boundary conditions, until a stationary state was reached. A nodalization of $109 \times 30 \times 30$, which amounts to 98100 nodes in total, was used and the results were taken at 40 seconds from the beginning of the simulation, when all of the macro-scale parameters such as net vapor generation, vapor mass flow rate out of the SG, presented in Figure 7.1, and total wall heat transfer rate indicated a converged state. Wall heat transfer rate and its division between the phases are shown in Figure 7.2. Computation time was 5 days on a single core of a 3.0 GHz quad-core Intel Xeon processor.

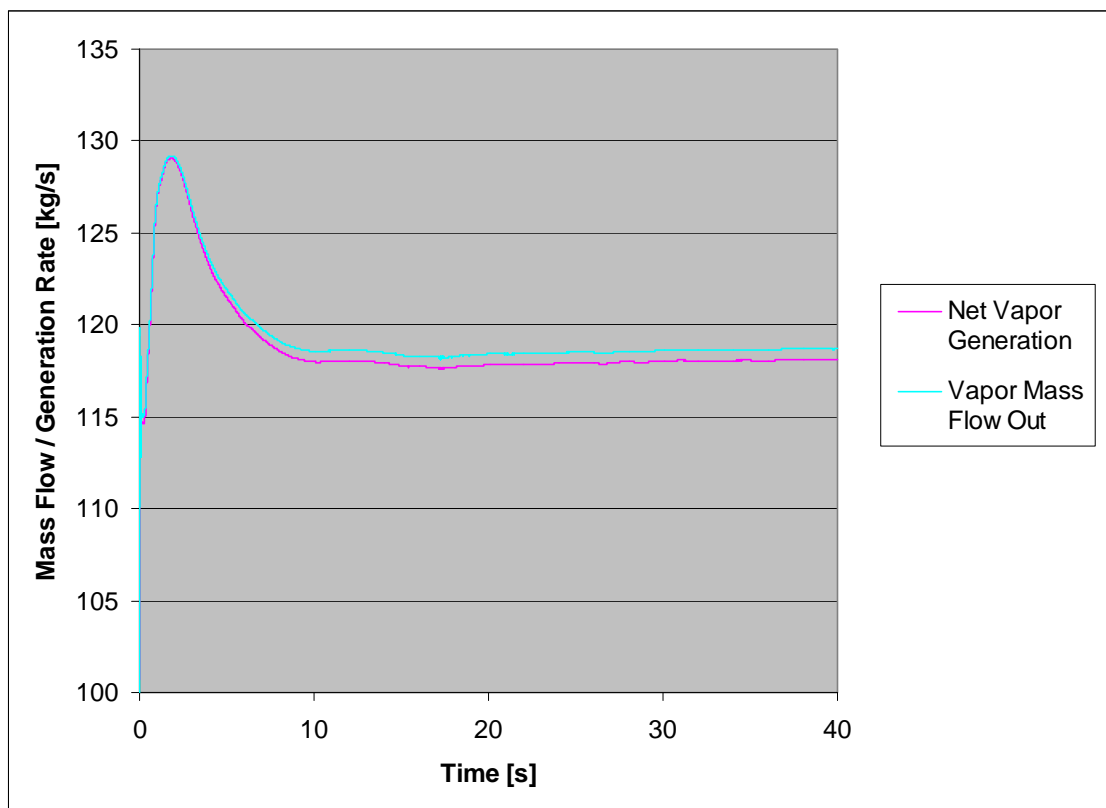


Figure 7.1: Net vapor generation and mass flow rate [kg/s].

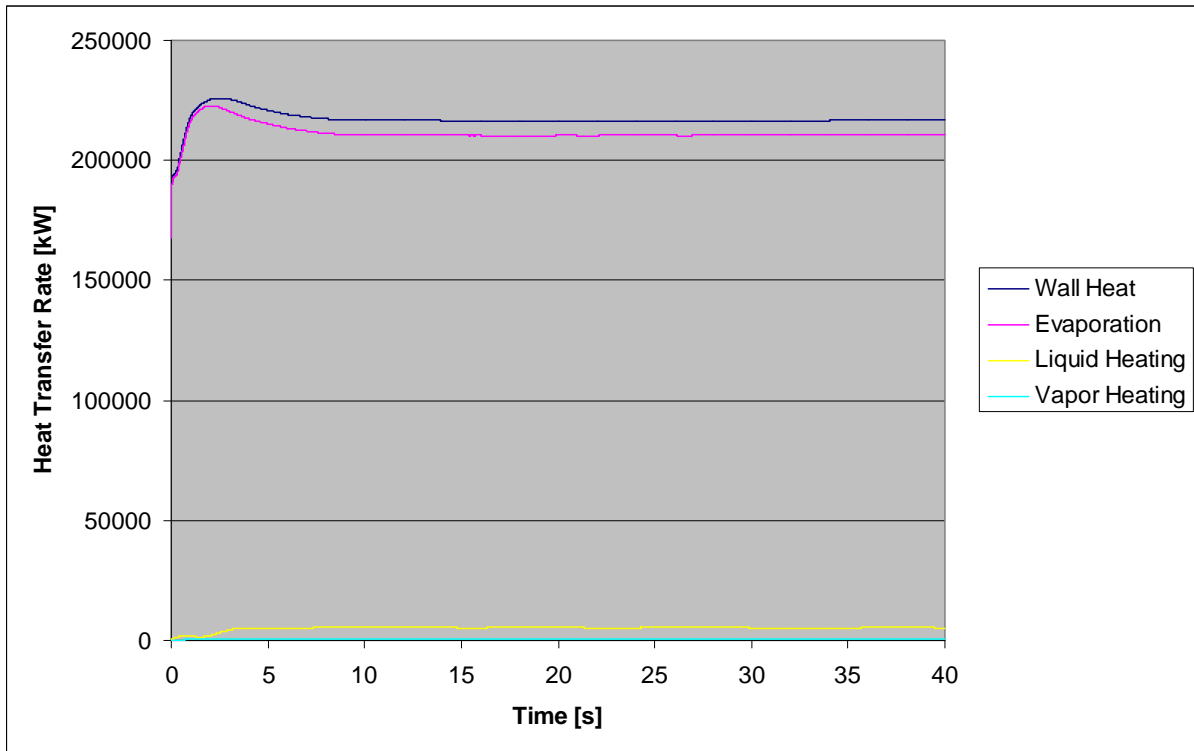


Figure 7.2: Division of wall heat transfer between the phases [kW].

At this point there were still some fluctuations between two sequential velocity fields, but it is quite hard to judge if the flow is still “evolving” towards a steady-state or if the nature of the flow in general is a transient one; so that these fluctuations would persist even if the simulation time was significantly increased. Liquid and vapor velocities, void fraction distribution and evaporation / condensation rate on yz-plane ($x = 2.83$ m) are presented in Figure 7.3 and evaporation / condensation rates on xz-plane ($y = 2.00$) and xy-plane ($z = 1.90$) in Figures 7.4 and 7.5, respectively. Liquid velocity, vapor velocity and void fraction are plotted on xz-plane, $y = 2.00$ and $y = 1.21$, in Figures 7.6 and 7.7.

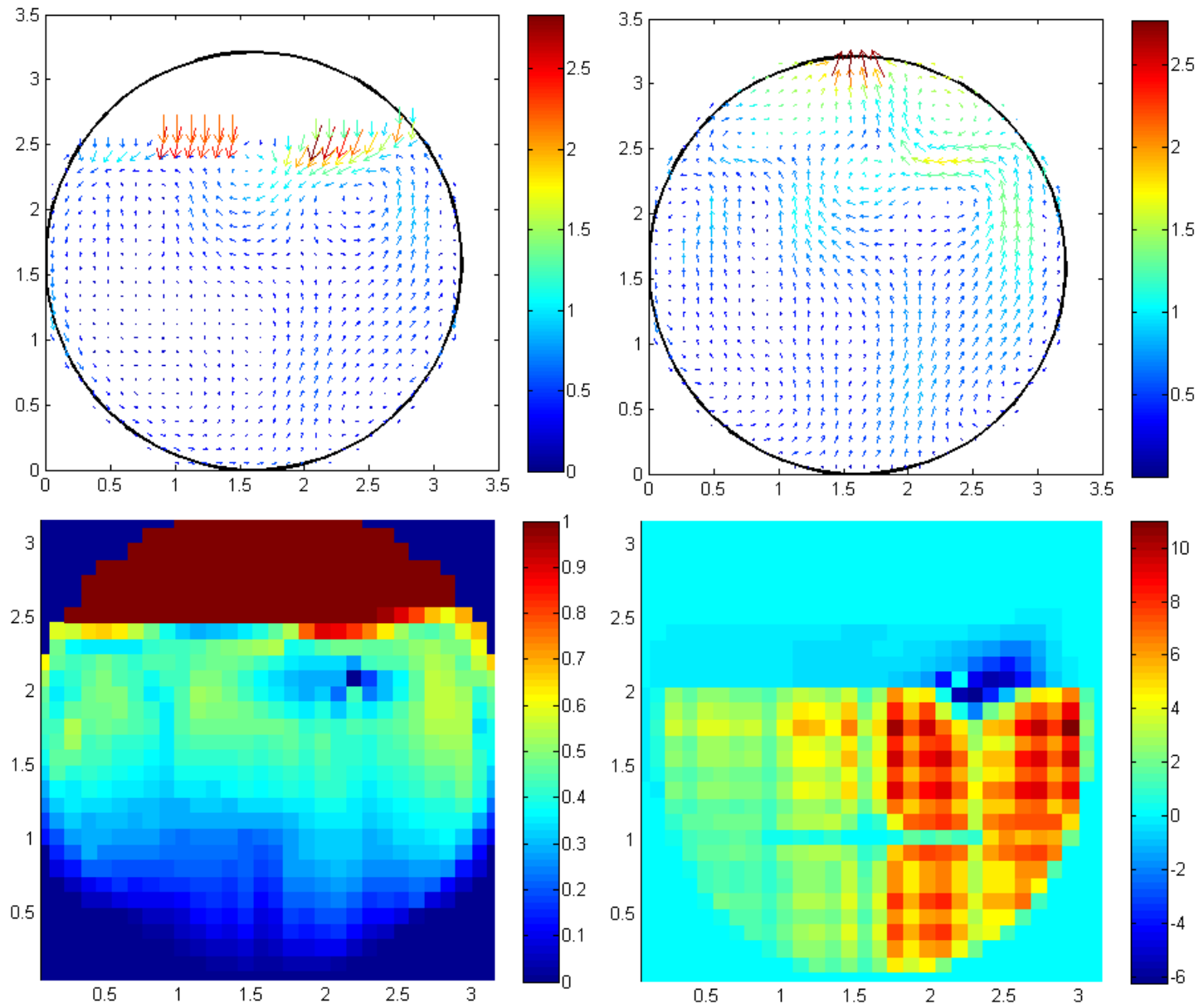


Figure 7.3: Liquid velocity (top left) [m/s], Vapor velocity (top right) [m/s], Void fraction (bottom left) [-] and Evaporation / Condensation rate (bottom right) [kg/m³s] on cross-section $x = 2.83$ m.

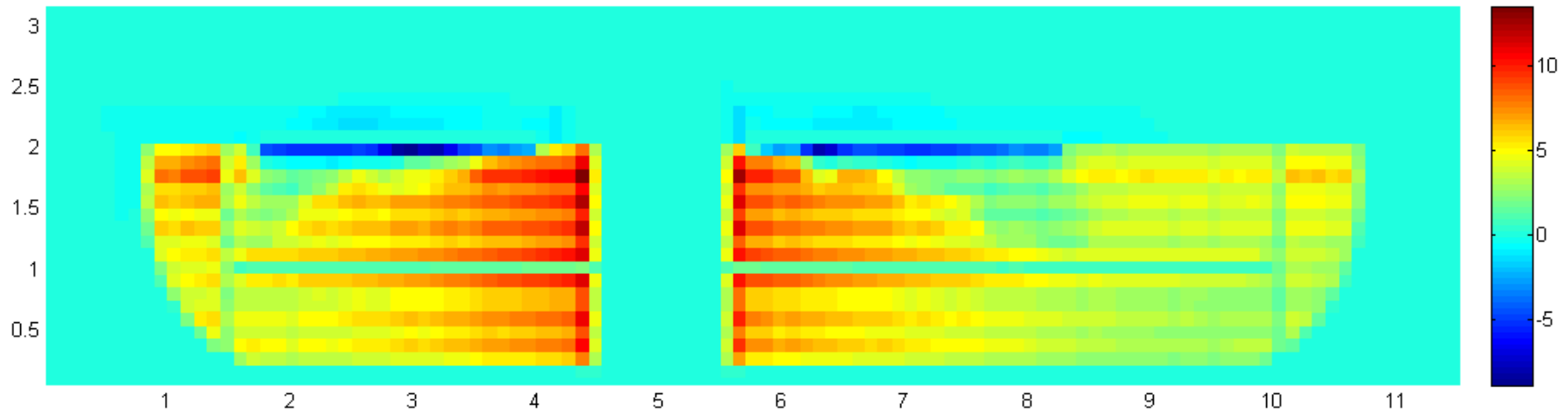


Figure 7.4: Evaporation / Condensation rate on xz-plane ($y = 2.00$) [$\text{kg}/\text{m}^3\text{s}$].

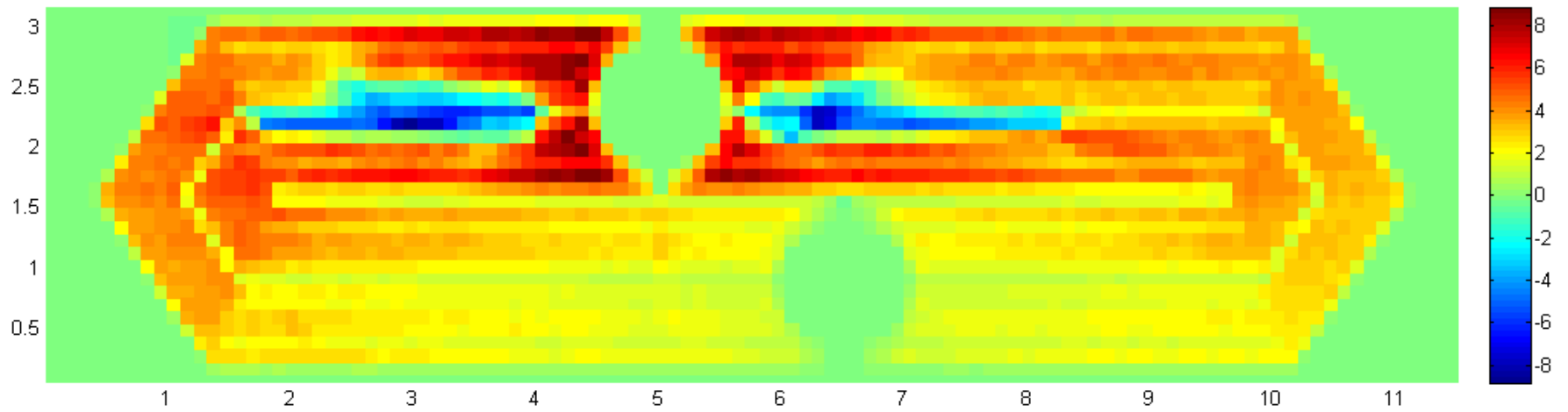


Figure 7.5: Evaporation / Condensation rate on xy-plane ($z = 1.90$) [$\text{kg}/\text{m}^3\text{s}$].

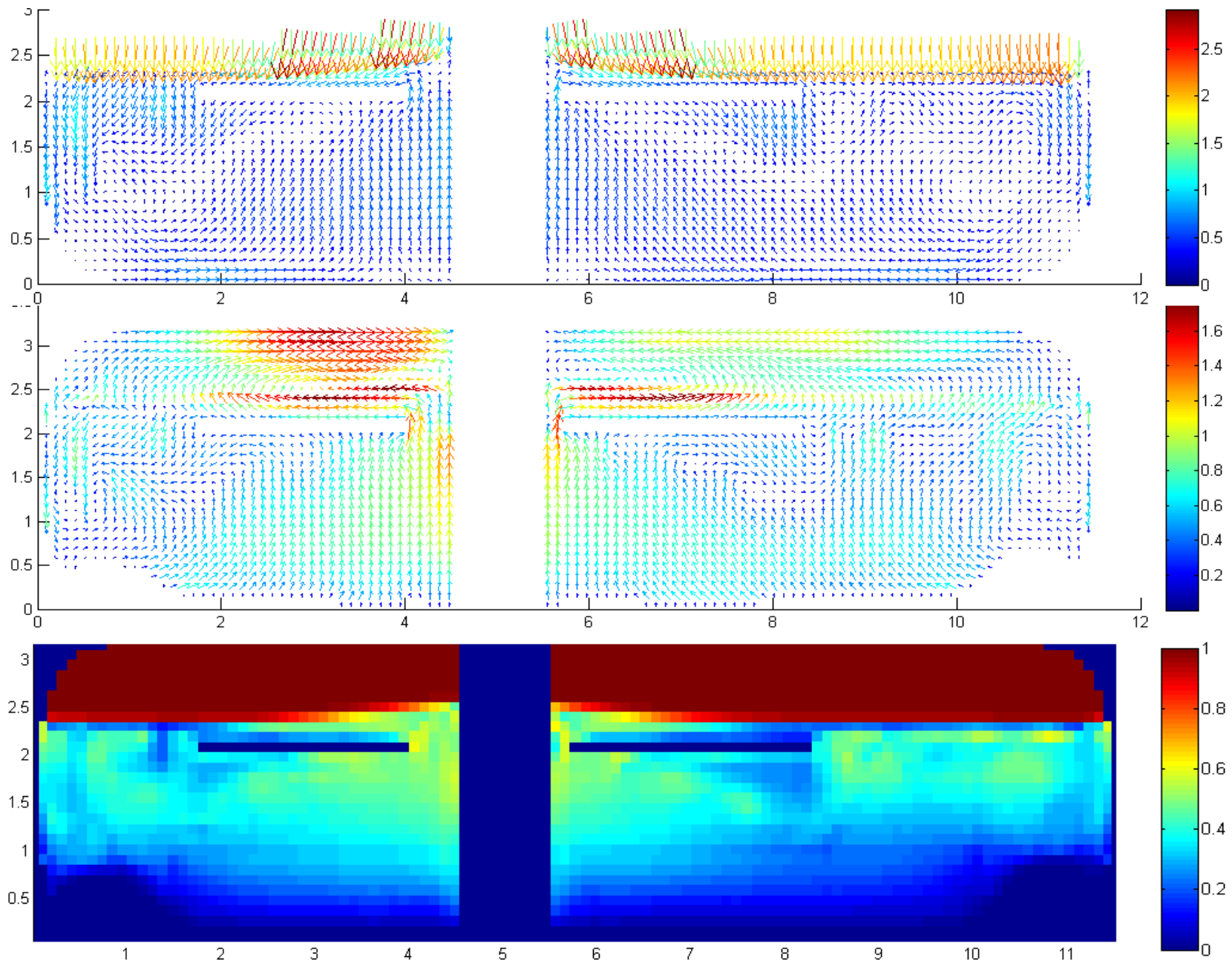


Figure 7.6: Liquid velocity (top) [m/s], Vapor velocity (middle) [m/s] and Void fraction (bottom) [-] on xz -plane ($y = 2.00$).

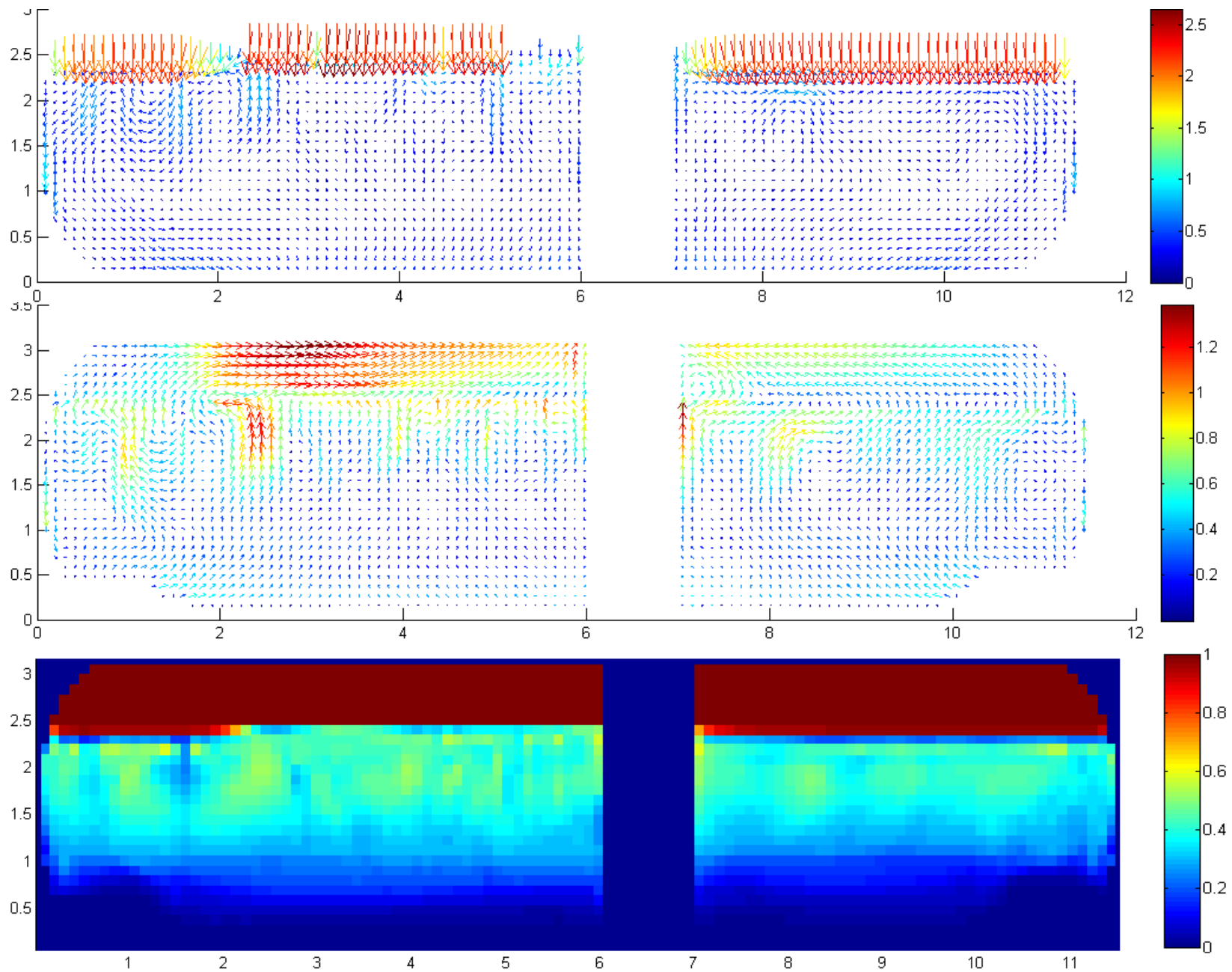


Figure 7.7: Liquid velocity (top) [m/s], Vapor velocity (middle) [m/s] and Void fraction (bottom) on xz-plane ($y = 1.21$).

8 Discussion of results

Velocity profiles in Figures 7.3, 7.6 and 7.7, in general, are quite expected; liquid flow is directed upwards in the space occupied by the primary tubes, especially on the hot side (the right-hand side of Figure 7.6 and cross-section $y = 2.00$), and downwards near the outer shell of the steam generator while strong vortices are formed at both ends of the steam generator; whereas vapor flow is directed mainly upwards throughout the whole steam generator, only in the vortices at the ends of the steam generator and near the feed water injection line is vapor flow diverted downwards (by the downwards flowing liquid).

There are, however, a couple of peculiarities: the most obvious of which is the existence of large liquid velocities, directed mainly downwards, at or near the water level. This could be caused by pressure gradients normal to the free surface of the liquid, together with the small liquid volume fractions above the surface, or this could be an artifact of the staggered grid; the averaging procedures could distort the results when volume fraction of one phase tends to zero. In any case, the cause of this should be closely studied. The other anomaly is that the flow field is generally quite erratic and there are many small vortices mostly in the liquid velocity fields, best seen in Figure 7.7. This is most likely, in part at least, due to the steep decrease in interphase drag coefficient to bubble diameter ratio after void fractions greater than 0.3 (Figure 4.1).

The void fraction distribution is quite satisfactory, apart from the film-like decrease in void fraction immediately below the water level (higher void fractions on both sides of the ‘film’). This may again be due to the averaging procedures necessary with staggered grids: as the staggered velocity nodes (of the vertical velocity components) occupy two consecutive nodes in the vertical direction and the values used in calculations of the vertical momentum are averaged from these two consecutive nodes, the void fraction distribution ‘seems’ (to the code) more uniform on the staggered grid than on the non-staggered grid.

The effect of the relatively cold feedwater, at 230 °C compared to saturated liquid at 257 °C, on evaporation / condensation rate is seen in Figures 7.3, 7.4 and 7.5; high condensation rates (negative values) occur near the feedwater injection line in a relatively compact area, and the cold feedwater doesn’t seem to penetrate, very far at least, into the tube bundles.

9 Comparison of results to Fluent simulations

A rough comparison of PORFLO simulation results to Fluent simulations, conducted in project SGEN (Rämä, 2009), are presented in this section. The closure laws are the same in both models; the same heat transfer and friction correlations were used; but the differences in the implementation, PORFLO being based on a structured, orthogonal Cartesian staggered grid and Fluent being based on a non-structured collocated grid, are difficult to account for. For easier comparison, void fraction distributions are plotted on yz-plane in Figure 9.1 and on xz-plane in Figure 9.2 for both Fluent and PORFLO simulations.

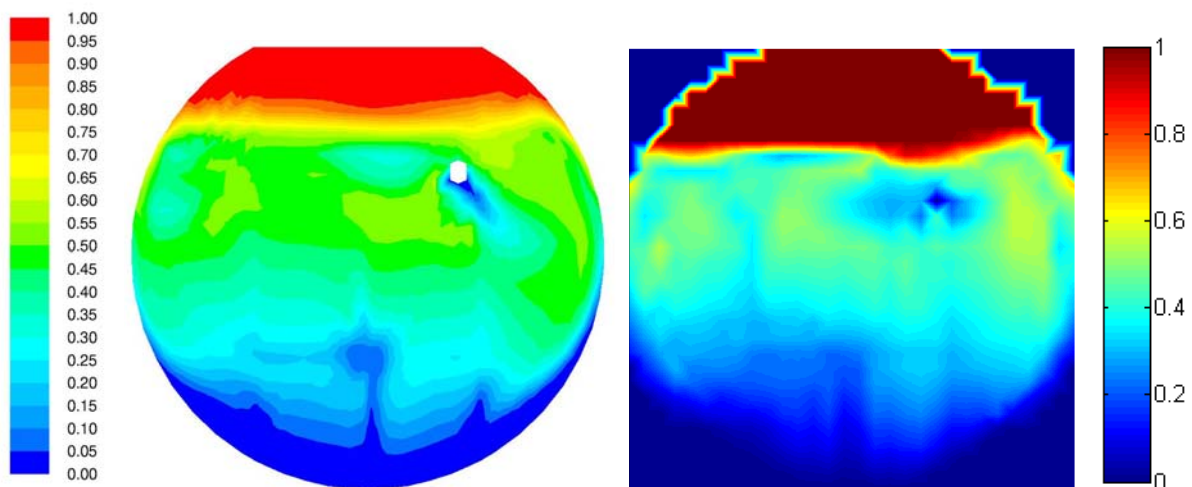


Figure 9.1: Comparison of void fraction distributions on cross-section $x = 2.83$ m between Fluent (left) and PORFLO (right).

The general outlook of the two void fraction distributions on cross-section $x = 2.83$, in Figure 9.1, is similar; smaller void fractions are located near the bottom, near the feedwater injection line, at the gaps between the tube sections, especially in the middle, and at the outer shell of the steam generator. One of the differences is the direction of the feedwater flow near the injection line; Fluent simulations suggest that the feedwater flow (at this cross-section at least) is directed downwards into the section occupied by the primary tubes, whereas PORFLO simulations would suggest that the colder feedwater more or less stays on top of the tube bundles and moves to the middle of the steam generator. This can be explained in part by the differences in the boundary conditions between the two cases; in Fluent simulations the feed water is injected downwards with a source term for the liquid momentum, whereas in PORFLO the liquid is injected as a mass source (into the appropriate nodes) without a source term for momentum. Appropriate momentum sources could be included in PORFLO as well, but in the absence of detailed data concerning the liquid velocity at the nozzles of the feedwater injection line, the momentum source terms were neglected all together. Another

difference between the results is that the shape of the water level is different; there is a distinct dip in the water level predicted by PORFLO directly above the feedwater injection line that is absent in the Fluent results. These two differences between the results may be linked; in Fluent simulations, as discussed above, the feedwater flow is directed further downwards, whereas in PORFLO simulations the cold feedwater is located directly below the dip in the surface level. The existence of cold feedwater near the surface may have a profound effect on the surface level at that point through increased condensation. At this point, however, it must be noted that on such coarse grids (grids with relatively similar coarseness were used in both cases) it is difficult to capture the surface level accurately.

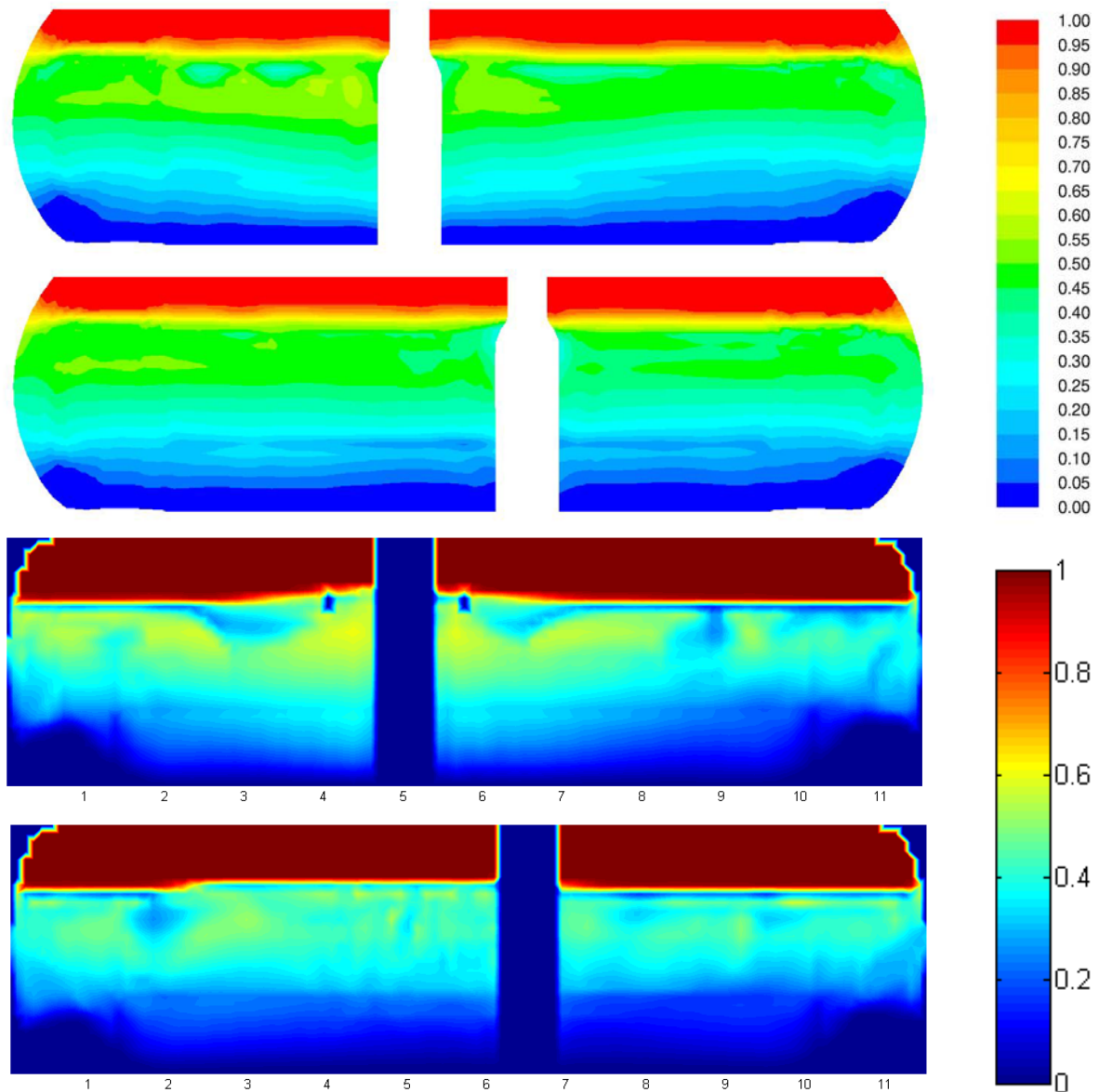


Figure 9.2: Comparison of void fraction distributions on cross-sections $y = 2.0$ m (upper) and $y = 1.21$ m (lower) between Fluent (on top) and PORFLO (below).

The void fraction distributions on cross-sections $y = 2.0$ and $y = 1.21$ m, in Figure 9.2, are more dissimilar than the cross-sections on yz -plane, in Figure 9.1. The “broad strokes” are similar in both cases; higher void fractions appear on the hot side (upper of the two pictures), especially near the hot collector, compared to the cold side and void fraction is increased when moving up from the bottom of the steam generator. The details that can be seen in both cases, however, are few. Generally speaking the distribution seems to be more uniform in the Fluent simulations than what is seen in PORFLO results. The numerous small pockets of higher void fractions, seen in the lower of the two PORFLO plots in Figure 9.2, stand out in particular.

References

- Groeneveld, D. C. and Snoek, C. W., 1986. A Comprehensive Examination of Heat Transfer Correlations Suitable for Reactor Safety Analysis. In: Hewitt, G. F., Delhaye, J. M. and Zuber, N., *Multiphase Science and Technology*, Vol. 2. Hemisphere. pp. 181-274. ISBN 0-89116-283-8
- Ilvonen, Mikko and Hovi, Ville, 2010. PORFLO development, applications and plans in 2008-2009. SAFIR2010 Research Programme, VTT Research report, VTT-R-01414-10. 27 p.
- Incropera, Frank P. and DeWitt, David P., 2002. *Fundamentals of Heat and Mass Transfer*, 5th edition. John Wiley & Sons, Inc. 981 p. ISBN 0-471-38650-2
- Ishii, M. and Zuber, N., 1979. Drag coefficient and relative velocity in bubbly, droplet or particulate flows. *American Institute of Chemical Engineers Journal*, Vol. 25, Issue 5, pp. 843-855
- Rämä, Tommi, 2009. Simulation of the Horizontal VVER-440 Steam Generator. Safir2010 report, (FNS-TERMO-144). 22 p.
- Simovic, Z. R., Ocokoljic S. and Stevanovic V. D., 2007. Interfacial friction correlations for the two-phase flow across tube bundle. *International Journal of Multiphase Flow*, Vol. 33, pp. 217-226